

An Analytic Method for the Kinematics and Dynamics of a Multiple-Backbone Continuum Robot

Regular Paper

Bin He^{1,*}, Zhipeng Wang¹, Qiang Li², Hong Xie² and Runjie Shen¹

¹ Department of Control Science & Engineering, Tongji University, Shanghai, China

² Institute of Advanced Manufacturing Technology, Tongji University, Shanghai, China

* Corresponding author E-mail: hebin@tongji.edu.cn

Received 7 Sep 2012; Accepted 3 Oct 2012

DOI: 10.5772/54051

© 2013 He et al.; licensee InTech. This is an open access article distributed under the terms of the Creative Commons Attribution License (<http://creativecommons.org/licenses/by/3.0>), which permits unrestricted use, distribution, and reproduction in any medium, provided the original work is properly cited.

Abstract Continuum robots have been the subject of extensive research due to their potential use in a wide range of applications. In this paper, we propose a new continuum robot with three backbones, and provide a unified analytic method for the kinematics and dynamics of a multiple-backbone continuum robot. The robot achieves actuation by independently pulling three backbones to carry out a bending motion of two-degrees-of-freedom (DoF). A three-dimensional CAD model of the robot is built and the kinematical equation is established on the basis of the Euler-Bernoulli beam. The dynamical model of the continuum robot is constructed by using the Lagrange method. The simulation and the experiment's validation results show the continuum robot can exactly bend into pre-set angles in the two-dimensional space (the maximum error is less than 5% of the robot length) and can make a circular motion in three-dimensional space. The results demonstrate that the proposed analytic method for the kinematics and dynamics of a continuum robot is feasible.

Keywords Continuum Robot, Multiple-Backbone Robot, Biologically Inspired Robot, Kinematics, Dynamics

1. Introduction

A continuum robot is a new type of biologically inspired robot. Compared to traditional rigid link robots, continuum robots feature a continuous backbone without joints [1], redundant degrees of freedom and exhibit significant compliance that provides exceptional operational capacities during environmental interaction and object manipulation. Due to inherent flexibility, a continuum robot has great potential in applications that include operation inside complex, unstructured environments [2-3], such as collapsed buildings in search and rescue operations [4-6] or minimally invasive surgery (MIS) in medical applications [7-10].

The outstanding compliance and adaptability of invertebrate limbs such as elephant trunks and octopus arms have motivated a recent surge of research activity in continuum robots [11]. Walker *et al.* designed a continuum robot inspired by the elephant trunk, which is actuated by a single flexible backbone with wires [10-13]. Simaan *et al.* presented a continuum robot with multiple flexible push-pull rods and derived a novel control

method based on force sensing [7-9, 15]. Webster III *et al.* proposed a novel continuum robot using the geometry and elastic interaction of precured concentric tubes to achieve a wide variety of shaft curves [16]. They put forward a framework for the kinematics of multi-link active cannulas and derived a set of differential equations that capture both bending and torsional effects continuously along the active cannulas backbone [17-19]. Trivedi *et al.* proposed a continuum robot with pneumatic actuation and derived an approach for modelling soft robotic manipulators that incorporates the effect of material nonlinearities, and distributed weight and payload [20].

There also has been much research into dynamical models of biologically inspired robot manipulators. Chirikjian developed an efficient formulation of approximate hyper-redundant manipulator dynamics, based on the principle of continuum mechanics [21]. Matsuno *et al.* presented the dynamic modelling of an underwater snake-like robot, based on the Newton-Euler equations [22]. The two methods considered hyper-redundant serial rigid-link systems, but cannot model the continuous nature of continuum robots. Gravagne *et al.* proposed a large-deflection dynamic model [23-24]. But this kind of dynamic modelling cannot be used in the case of general three dimensions. In [25] and [26], Mochiyama *et al.* developed a three-dimensional dynamic model for an inextensible (constant length) continuum manipulator based on a slice of the arm, which is regarded as a rigid link with an infinitesimal width of a serial rigid chain manipulator. However, the dynamic model does not include extensible manipulators. Tatlicioglu put forward a new dynamic model for continuum robot manipulators by using the geometric model of extensible continuum robot manipulators with no torsional effects [27-28].

In this paper, a novel continuum robot with three backbones was proposed and provided a new analytic method based on the Euler-Bernoulli beam for kinematics and dynamics of a robot. In Section 2, a new wire-driven continuum robot using super-elastic NiTi alloy is presented. Then the kinematics of the continuum robot is analysed on the basis of the Euler-Bernoulli beam in Section 3. By using the Lagrange method, the dynamical model of the robot is obtained in Section 4. Simulation results are presented in Section 5. Experiments on the performance of the robot are described in Section 6. Finally, conclusions and future work are reported in Section 7.

2. Design of the robot and modelling assumptions

Fig. 1 shows the structure of the continuum robot, which is composed of a base disk, an end disk, several spacer disks and four super elastic NiTi wires as its backbones.

The central wire is the primary backbone and the remaining three wires are secondary backbones. The secondary backbones are equidistant from the primary backbone and from each other. The central backbone is glued to all the disks, while the secondary backbones are only attached to the end disk and are free to slide through appropriately tolerated holes in the base and spacer disks. The secondary backbones are used for actuating the continuum robot. The spacer disks are distributed uniformly to prevent buckling of the central and secondary backbones and to maintain an equal distance between the secondary backbones and the central backbone. Through independent actuation of the three secondary backbones, a 2-DoF bending motion of the continuum robot can be achieved. The multi-DoF continuum robot can be realized by using series 2-DoF unit.

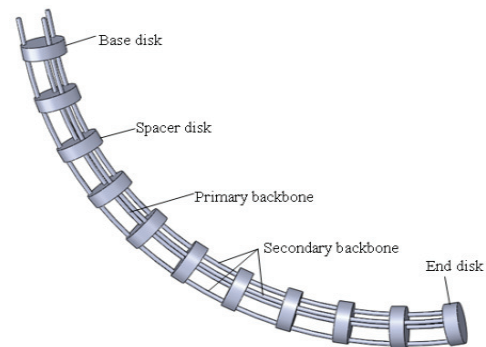


Figure 1. Continuum robot CAD drawing.

The modelling assumptions of the continuum robot are summarized as follows.

1. The super elastic NiTi wire is assumed to have linear and isotropic relations between strain and stress [29] in the presented robot. The only external force acting on the continuum robot is driving force and the backbones behave like Euler-Bernoulli beams [9].
2. The robot disks are thin and rigid and friction between the backbones and the disks is neglected [9].
3. Compared to the elastic deformation energy, gravitational potential energy is much smaller. Gravity can be ignored in the analysis.
4. The shape of continuum robot is assumed to be a smooth and continuous curve and each backbone has constant curvature.
5. The robot is under static equilibrium [15].
6. The primary and the secondary backbones are always perpendicular to the base, the spacer and the end disks.

3. Kinematics analysis

3.1 Flexible beam with end-moment

Fig. 2 shows a flexible beam with an applied moment (M) at the free end. The angular rotation at the beam end is

θ_A . l is the length of the flexible beam. $P(x, y)$ is any point located at the flexible beam, with the length away from origin point O as s and its corresponding angular rotation is θ_p . The position and orientation of the point P can be obtained based on the Euler-Bernoulli beam equation [30].

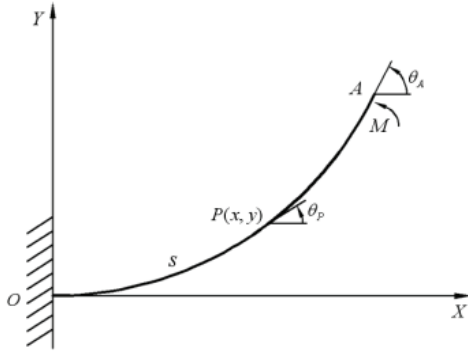


Figure 2. The beam with end-moment.

$$\begin{cases} x = \frac{EI}{M} \sin \theta_p \\ y = \frac{EI}{M} (1 - \cos \theta_p) \\ \theta_p = \frac{Ms}{EI} \end{cases} \quad \text{or} \quad \begin{cases} x = \frac{s}{\theta_p} \sin \theta_p \\ y = \frac{s}{\theta_p} (1 - \cos \theta_p) \end{cases} \quad (1)$$

where, EI is the stiffness of flexible beam.

According to assumption (4), we can get the follow equation:

$$\frac{s}{\theta_p} = \frac{l}{\theta_A} \quad (2)$$

3.2 Kinematic nomenclature

According to the structural characteristics of a continuum robot, it can be considered as a flexible beam. Fig. 3 shows the continuum robot with only the primary and two secondary backbones illustrated. There are three coordinate systems defined [8]: (1) the base disk coordinate system $\{X, Y, Z\}$, (2) the bending plane coordinate system $\{X_1, Y_1, Z_1\}$, (3) the end disk coordinate system $\{X_e, Y_e, Z_e\}$. The base disk coordinate system is attached to the base disk. The X axis points from the centre to the first secondary backbone, the Z axis is perpendicular to the disk, and the Y axis is established according to the "right-hand rule". The bending plane coordinate system can be obtained by rotating the base disk coordinate around the Z axis for angle γ . The end disk coordinate system is obtained from the base disk coordinate system by four steps: (1) translating the centre O to O_e , (2) rotating the local coordinate around its Z axis for angle γ , (3) rotating the local coordinate around its Y axis for angle β , (4) rotating the local coordinate around its Z axis for angle $-\gamma$.

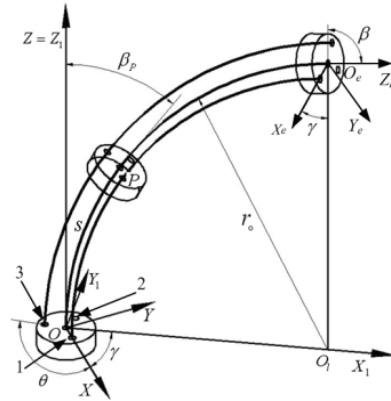


Figure 3. The geometric model of a continuum robot (a secondary backbone is omitted for clear illustration).

The following symbols are used:

s - arc-length parameter of the segment OP ($s=0$ at the base disk and $s=l$ at the end disk).

r - the distance from the primary backbone to each secondary backbone on the disk.

r_o - curvature radius of the primary backbone, defined in the bending plane.

β_p - the bending angle of the primary backbone tangent in the X_1Z_1 plane at the point P . β is the bending angle at the end disk.

γ - the rotation angle of the bending plane.

θ - division angle ($\theta = 2\pi / n$, is the number of secondary backbones).

m_1 - the total mass of the primary backbone.

m_2 - the total mass of the secondary backbone.

h - distance between adjacent disks.

The kinematics analysis consists of two transformation parts: (1) transformation between joint space and operational space; (2) transportation between driving space and joint space.

3.3 Transformation between joint space and operational space

According to Eq. (2), we can get the equation as follows:

$$\beta_p = \frac{s\beta}{l} \quad (3)$$

Based on the flexible beam model, as mentioned above, the position of point P can be obtained as follows:

$$\begin{cases} x_1 = \frac{s}{\beta_p} (1 - \cos \beta_p) \\ y_1 = 0 \\ z_1 = \frac{s}{\beta_p} \sin \beta_p \end{cases} \quad (4)$$

The coordinates of point P in the bending plane coordinate system can be translated into the base disk coordinate system as follows:

$$\begin{bmatrix} x \\ y \\ z \end{bmatrix} = \text{Rot}(Z, \gamma)^{-1} \begin{bmatrix} x_1 \\ y_1 \\ z_1 \end{bmatrix} \quad (5)$$

where, $\text{Rot}(Z, \gamma)$ is given by:

$$\text{Rot}(Z, \gamma) = \begin{bmatrix} \cos \gamma & -\sin \gamma & 0 \\ \sin \gamma & \cos \gamma & 0 \\ 0 & 0 & 1 \end{bmatrix} \quad (6)$$

The position of any point P on the primary backbone can be expressed as:

$$P = \begin{bmatrix} x & y & z \end{bmatrix}^T = \begin{bmatrix} \frac{s}{\beta_p}(1 - \cos \beta_p) \cos \gamma & \frac{s}{\beta_p}(1 - \cos \beta_p) \sin \gamma & \frac{s}{\beta_p} \sin \beta_p \end{bmatrix}^T \quad (7)$$

Substituting Eq. (3) for Eq. (7), the coordinates of point P in the base disk coordinate system can be given by:

$$P = \begin{bmatrix} x & y & z \end{bmatrix}^T = \begin{bmatrix} \frac{s}{\beta_p}(1 - \cos \beta_p) \cos \gamma & \frac{s}{\beta_p}(1 - \cos \beta_p) \sin \gamma & \frac{s}{\beta_p} \sin \beta_p \end{bmatrix}^T \quad (8)$$

The rotation matrix can be written as:

$$R = \text{Rot}(Z, \gamma) \text{Rot}(Y, \beta) \text{Rot}(Z, -\gamma) = \begin{bmatrix} c^2 \gamma c \beta + s^2 \gamma & c \gamma s \gamma c \beta - c \gamma s \gamma & c \gamma s \beta \\ c \gamma s \gamma c \beta - c \gamma s \gamma & s^2 \gamma c \beta + c^2 \gamma & s \gamma s \beta \\ -c \gamma s \beta & -s \gamma s \beta & c \beta \end{bmatrix} \quad (9)$$

where, $s\beta = \sin \beta$, $c\beta = \cos \beta$, the interval of the bending angle β is $[0, \pi]$; $s\gamma = \sin \gamma$, $c\gamma = \cos \gamma$, the interval of the rotation angle γ is $[0, 2\pi]$.

The transformation matrix from the end disk coordinate system to the base coordinate system can consist of Eqs. 8 and 9 and be expressed as:

$$T = \begin{bmatrix} R & P \\ 0 & 1 \end{bmatrix} \quad (10)$$

3.4 Transformation between joint space and driving space

In the motion of the continuum robot, the position and shape can be controlled by changing the lengths of the three driving NiTi wires, which are equally spaced by 120 degrees around the primary backbone, as shown in Fig. 4. r_i $\{i=1, 2, 3\}$ represents the curvature radius of each second backbone. The change in length of each wire is realized by a stepping motor and the motion of each motor is directly proportional to the displacement of the wires.

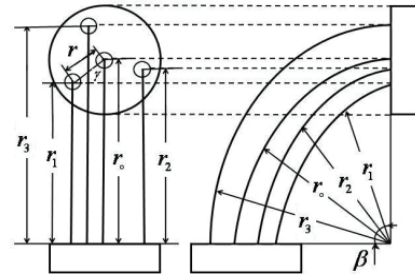


Figure 4. Driving wires model.

The transformation between driving space and joint space can be expressed as:

$$\begin{cases} q_1 = r\beta \cos(\gamma) \\ q_2 = r\beta \cos(-\gamma + \theta) \\ q_3 = r\beta \cos(\gamma + \theta) \end{cases} \quad (11)$$

where, q_i $\{i=1, 2, 3\}$ is the length of each driving wire and r is the distance from each secondary backbone to the primary backbone (the secondary backbones are equidistant from the primary backbone), and $\theta = 2\pi/3$.

4. Dynamics analysis

4.1 Kinetic energy of the continuum robot

The structure of the continuum robot consists of a primary backbone, a secondary backbone and disks. So the kinetic energy of the continuum robot should consist of these three parts.

Firstly, the kinetic energy of the primary backbone can be obtained. Calculating the derivative of the Eq. (8), the velocity of point P can be expressed as follows:

$$\begin{cases} \frac{dx}{dt} = \frac{1}{\beta} [s \sin \frac{s\beta}{l} \cos \gamma - \frac{l}{\beta} (1 - \cos \frac{s\beta}{l}) \cos \gamma] \frac{d\beta}{dt} \\ \quad - \frac{l}{\beta} (1 - \cos \frac{s\beta}{l}) \sin \gamma \frac{d\gamma}{dt} \\ \frac{dy}{dt} = \frac{1}{\beta} [s \sin \frac{s\beta}{l} \sin \gamma - \frac{l}{\beta} (1 - \cos \frac{s\beta}{l}) \sin \gamma] \frac{d\beta}{dt} \\ \quad + \frac{l}{\beta} (1 - \cos \frac{s\beta}{l}) \cos \gamma \frac{d\gamma}{dt} \\ \frac{dz}{dt} = \frac{1}{\beta} (s \cos \frac{s\beta}{l} - \frac{l}{\beta} \sin \frac{s\beta}{l}) \frac{d\beta}{dt} \end{cases} \quad (12)$$

The kinetic energy of the primary backbone can be obtained as:

$$E_{k1} = \frac{1}{2} \int_0^l [(\frac{dx}{dt})^2 + (\frac{dy}{dt})^2 + (\frac{dz}{dt})^2] \rho A ds \quad (13)$$

where ρ is the density of the primary backbone and A is the cross-section area of the primary backbone.

Substituting Eq. (12) for Eq. (13), we can obtain the following:

$$E_{k1} = \frac{1}{6} m_1 l^2 \left(\frac{d\beta}{dt} \right)^2 K_1 + \frac{1}{8} m_1 l^2 \left(\frac{d\gamma}{dt} \right)^2 K_2 \quad (14)$$

$$K_1 = (\beta^3 + 6\beta - 12\sin\beta + 6\beta\cos\beta) / \beta^5 \quad (15)$$

$$K_2 = (6\beta - 8\sin\beta + \sin 2\beta) / \beta^3 \quad (16)$$

where m_1 is the mass of the primary backbone and K_1 and K_2 are the kinetic energy equivalent factor.

From Eq. (15) and (16), we can see that K_1 and K_2 can be expressed as a function of bending angle β . The two equations can be simplified by using least square fit, as shown in the following:

$$K_1 = -0.00426\beta^2 - 0.00277\beta + 0.15085 \quad (17)$$

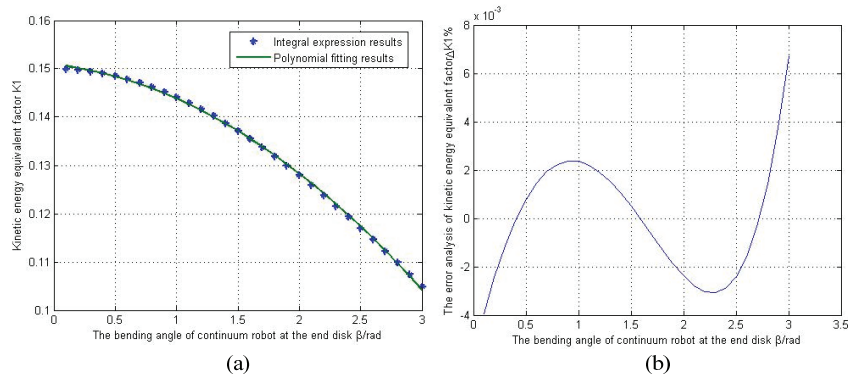


Figure 5. The comparison and error analysis of kinetic energy equivalent factor K_1 . (a) The comparison of the kinetic energy equivalent factor. (b) The error analysis of the kinetic energy equivalent factor.

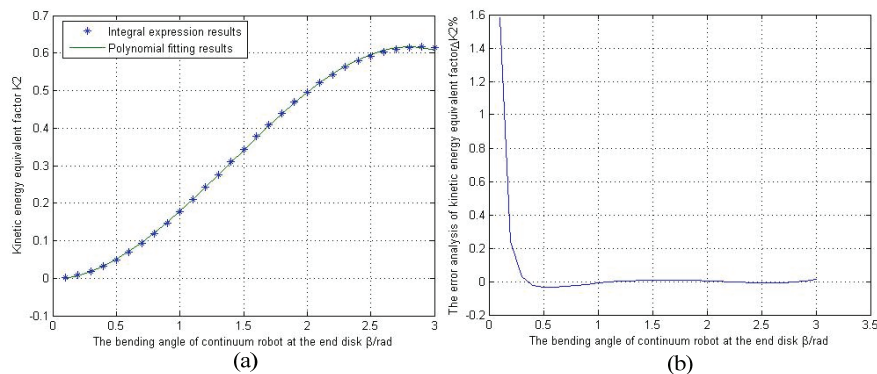


Figure 6. The comparison and error analysis of kinetic energy equivalent factor K_2 . (a) The comparison of the kinetic energy equivalent factor. (b) The error analysis of the kinetic energy equivalent factor.

Secondly, the kinetic energy of the secondary backbone, which consists of two parts, can be obtained. One part of the kinetic energy of the secondary backbone is the same as with the primary backbone. Another part of the kinetic energy comes from driven kinetic energy.

From Eq. (12), the first part of the kinetic energy can be expressed as:

$$E_{k11} = \frac{3}{2} \int_0^l \left[\left(\frac{dx}{dt} \right)^2 + \left(\frac{dy}{dt} \right)^2 + \left(\frac{dz}{dt} \right)^2 \right] \rho A ds \quad (19)$$

$$K_2 = -0.05567\beta^3 + 0.2328\beta^2 + 0.006216\beta - 0.00406 \quad (18)$$

Fig. 5 and 6 show the comparison and error analysis of the kinetic energy equivalent factor. From Fig. 5(a) and 6(a), we can see that the fitting curves are closely consistent with the actual curve. Fig. 5(b) shows that the calculated relative error of the kinetic energy equivalent coefficient is less than 0.8%, which indicates that the simplified expression is very accurate. The continuum robot has a small deflection near the base disk, which makes the relative error slightly larger, as shown in Fig. 6(b). But when the rotation angle $\beta > 0.5 \text{ rad}$, the relative error becomes smaller. According to the above analysis, the simplifications of the kinetic energy equivalent factors are available.

where ρ is the density of the secondary backbone and A is the cross-section area of the secondary backbone.

By combining Eq. (12) and (19) we can get the following equation:

$$E_{k11} = \frac{1}{2} m_1 l^2 \left(\frac{d\beta}{dt} \right)^2 K_1 + \frac{3}{8} m_1 l^2 \left(\frac{d\gamma}{dt} \right)^2 K_2 \quad (20)$$

where m_1 is the mass of the secondary backbone, K_1 and K_2 are kinetic energy equivalent factors (as mentioned above).

Calculating the derivative of Eq. (11), the driven velocity can be given as:

$$\begin{cases} \frac{dq_1}{dt} = r \cos(\gamma) \frac{d\beta}{dt} - r \beta \sin(\gamma) \frac{d\gamma}{dt} \\ \frac{dq_2}{dt} = r \cos(-\gamma + \theta) \frac{d\beta}{dt} + r \beta \sin(-\gamma + \theta) \frac{d\gamma}{dt} \\ \frac{dq_3}{dt} = r \cos(\gamma + \theta) \frac{d\beta}{dt} - r \beta \sin(\gamma + \theta) \frac{d\gamma}{dt} \end{cases} \quad (21)$$

Then the driven kinetic energy of the secondary backbone can be obtained as follows:

$$E_{k22} = \frac{1}{2} m_1 \left[\left(\frac{dq_1}{dt} \right)^2 + \left(\frac{dq_2}{dt} \right)^2 + \left(\frac{dq_3}{dt} \right)^2 \right] \quad (22)$$

Substituting Eq. (21) for Eq. (22), we can get the following equations:

$$E_{k22} = \frac{1}{2} m_1 \left[K_3 \left(\frac{d\beta}{dt} \right)^2 + K_4 \frac{d\beta}{dt} \frac{d\gamma}{dt} + K_5 \left(\frac{d\gamma}{dt} \right)^2 \right] \quad (23)$$

$$K_3 = r^2 [\cos^2(\gamma) + \cos^2(-\gamma + \theta) + \cos^2(\gamma + \theta)] \quad (24)$$

$$K_4 = r^2 \beta [-\sin 2\gamma + \sin 2(-\gamma + \theta) - \sin 2(\gamma + \theta)] \quad (25)$$

$$K_5 = r^2 \beta^2 [\sin^2(\gamma) + \sin^2(-\gamma + \theta) + \sin^2(\gamma + \theta)] \quad (26)$$

where m_1 is the mass of the secondary backbone and K_3 , K_4 and K_5 are kinetic energy equivalent factors.

Combining Eq. (20) and (23), the total kinetic energy of the secondary backbone can be written as:

$$E_{k2} = \frac{1}{2} m_1 (l^2 K_1 + K_3) \left(\frac{d\beta}{dt} \right)^2 + \frac{1}{8} m_1 (3l^2 K_2 + 4K_5) \left(\frac{d\gamma}{dt} \right)^2 + \frac{1}{2} m_1 K_4 \frac{d\beta}{dt} \frac{d\gamma}{dt} \quad (27)$$

Thirdly, the kinetic energy of the spacer and end disks can be obtained. All disks are attached to the primary backbone, so the velocity of the disks can be derived from Eq. (8). The velocity of every disk can be expressed as:

$$\begin{cases} \frac{dx}{dt} = \frac{1}{\beta} \left[kh \sin \frac{kh\beta}{l} \cos \gamma - \frac{l}{\beta} \left(1 - \cos \frac{kh\beta}{l} \right) \cos \gamma \right] \frac{d\beta}{dt} \\ \quad - \frac{l}{\beta} \left(1 - \cos \frac{kh\beta}{l} \right) \sin \gamma \frac{d\gamma}{dt} \\ \frac{dy}{dt} = \frac{1}{\beta} \left[kh \sin \frac{kh\beta}{l} \sin \gamma - \frac{l}{\beta} \left(1 - \cos \frac{kh\beta}{l} \right) \sin \gamma \right] \frac{d\beta}{dt} \\ \quad + \frac{l}{\beta} \left(1 - \cos \frac{kh\beta}{l} \right) \cos \gamma \frac{d\gamma}{dt} \\ \frac{dz}{dt} = \frac{1}{\beta} \left(kh \cos \frac{kh\beta}{l} - \frac{l}{\beta} \sin \frac{kh\beta}{l} \right) \frac{d\beta}{dt} \end{cases} \quad (28)$$

where $k=1, 2, 3 \dots, n$ is the total number of spacer and end disks ($n=l/h$).

The total kinetic energy of all the spacer and end disks can be expressed as:

$$E_{k3} = \sum_{k=1}^n \frac{1}{2} m_2 \left[\left(\frac{dx}{dt} \right)^2 + \left(\frac{dy}{dt} \right)^2 + \left(\frac{dz}{dt} \right)^2 \right] \quad (29)$$

By combining Eq. (28) and (29), we have the following equation:

$$E_{k3} = \frac{1}{2} m_2 \left(\frac{d\beta}{dt} \right)^2 K_6 + \frac{1}{2} m_2 \left(\frac{d\gamma}{dt} \right)^2 K_7 \quad (30)$$

$$K_6 = \frac{h^2 n(n+1)(2n+1)}{6\beta^2} + (2n+1) \frac{l^2}{\beta^4} - \frac{l^2}{\beta^4} \frac{\sin \beta + \sin \frac{(n+1)\beta}{n}}{\sin \frac{\beta}{n}} \quad (31)$$

$$K_7 = \frac{l^2}{\beta^2} \left[\frac{3n}{2} + \frac{3}{4} - \frac{hl}{\beta^3} \frac{(n+1)\sin \beta - n \sin \frac{(n+1)\beta}{n}}{2 \sin^2 \frac{\beta}{2n}} - \frac{\sin \beta + \sin \frac{(n+1)\beta}{n}}{\sin \frac{\beta}{n}} + \frac{\sin 2\beta + \sin \frac{2(n+1)\beta}{n}}{4 \sin \frac{2\beta}{n}} \right] \quad (32)$$

where, m_2 is the mass of a disk and K_6 and K_7 are kinetic energy equivalent factors.

From Eq. (31) and (32), when n and h are determined, the kinetic energy equivalent factors K_6 and K_7 can be expressed as a function of bending angle β . Assuming that $n=10$ and $h=15\text{mm}$, the form of K_6 and K_7 can be simplified by using least square fit, shown as follows:

$$K_6 = -0.00043\beta^2 - 0.00031\beta + 0.01435 \quad (33)$$

$$K_7 = -0.00394\beta^3 + 0.01575\beta^2 + 0.00131\beta - 0.00047 \quad (34)$$

Fig. 7 and 8 show the comparison and error analysis of the kinetic energy equivalent factors. They look similar to Fig. 5 and 6. From Fig. 7(a) and 8(a), we can see that the fitting curves are very consistent with the actual curve. Fig. 7(b) shows that the calculated relative error of the kinetic energy equivalent coefficient is close to zero. It indicates that the simplified expression is very accurate. From Fig. 8(b) we can see that when the rotation angle β is smaller, the relative error is slightly larger. But when the rotation angle $\beta > 0.5\text{rad}$, the relative error is less than 0.01%. The analysis from the above proves that the simplifications of the kinetic energy equivalent factors are feasible.

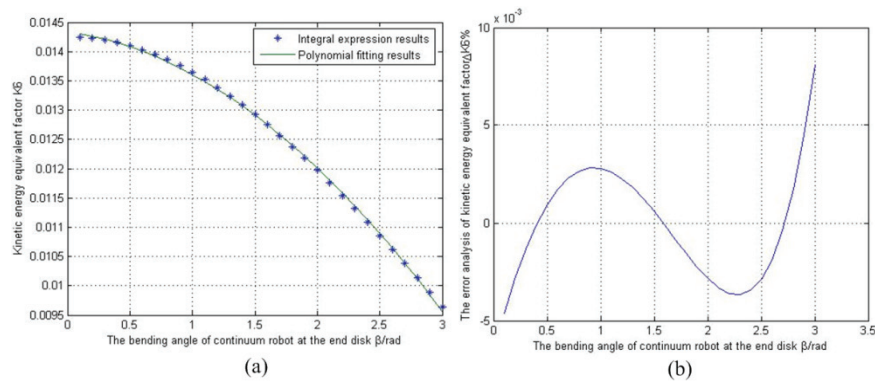


Figure 7. The comparison and error analysis of kinetic energy equivalent factor K_6 . (a) The comparison of the kinetic energy equivalent factor. (b) The error analysis of the kinetic energy equivalent factor.

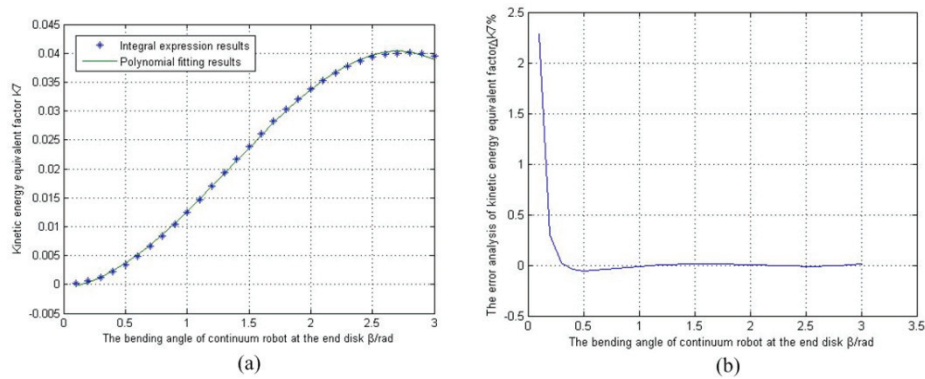


Figure 8. The comparison and error analysis of kinetic energy equivalent factor K_7 . (a) The comparison of the kinetic energy equivalent factor. (b) The error analysis of the kinetic energy equivalent factor.

By combining Eq. (14), (27) and (30), the total kinetic energy of continuum robot can be obtained as follows:

$$E_k = \frac{1}{6}(4m_1l^2K_1 + 3m_1K_3 + 3m_2K_6)\left(\frac{d\beta}{dt}\right)^2 + \frac{1}{2}(m_1l^2K_2 + m_1K_5 + m_2K_7)\left(\frac{d\gamma}{dt}\right)^2 + \frac{1}{2}m_1K_4\frac{d\beta}{dt}\frac{d\gamma}{dt} \quad (35)$$

4.2 Potential energy of the continuum robot

For a continuum robot, the potential energy consists of two parts: elastic potential energy and gravitational potential energy. Relative to the elastic potential energy, its gravitational potential energy can be ignored. The reason will be shown in the following section.

Each disk of the continuum robot in Fig. 1 weighs 0.848g. The density of NiTi is 6.2 grams/cm³. It is assumed that the shape of the continuum robot is circular. The ratio of gravitational energy to elastic energy can be calculated and is a function of the bending angle β , which is plotted in Fig. 9. The maximum value of gravitational potential energy is less than 1.4% of the elastic deformation energy for the continuum robot. And it decreases with the increase of the bending angle β . So compared to the elastic deformation energy, the gravitational potential energy can be ignored. The conclusion proves the feasibility of assumption (3).

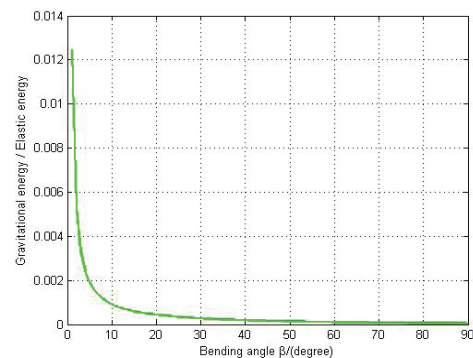


Figure 9. Relationship between the bending angle β and gravitational energy over elastic energy ratio.

The elastic energy of the continuum robot is given by [31]:

$$E_p = 4 \int_0^l \frac{EI}{2} \left(\frac{d\beta_p}{ds} \right)^2 ds = \frac{2EI}{l} \beta^2 \quad (36)$$

where EI is the stiffness of NiTi alloy wire, $\beta_p = s\beta/l$ as mentioned above.

4.3 Generalized force of the continuum robot

Generalized force is a force or torque acting on the generalized coordinates. As the robot has two degrees of

freedom, the pose of the continuum robot can be determined by two driving forces. The structure of continuum robot is centrosymmetric, as shown in Fig. 10. So the driving force F_1 , F_2 and F_3 have the characteristic of space rotation symmetric. The robot achieves actuation by independently pulling two backbones at the same time. The following formulas are derived based on the assumption that F_1 and F_2 take effect.

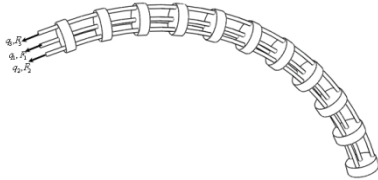


Figure 10. Driving diagrammatic sketch of the continuum robot.

Given the displacement of driving force F_1 and F_2 are q_1 and q_2 , respectively. q_i can be defined as $l-l_i$, where l is the length of the primary backbone and l_i is the length of secondary backbone. The generalized force of the continuum robot can be expressed as:

$$\begin{cases} Q_1 = F_1 \frac{\partial q_1}{\partial \beta} + F_2 \frac{\partial q_2}{\partial \beta} \\ Q_2 = F_1 \frac{\partial q_1}{\partial \gamma} + F_2 \frac{\partial q_2}{\partial \gamma} \end{cases} \quad (37)$$

From Eq. (11) and (37), we can get the following equations:

$$\begin{cases} Q_1 = F_1 r \cos(\gamma) + F_2 r \cos(-\gamma + \theta) \\ Q_2 = -F_1 r \beta \sin(\gamma) + F_2 r \beta \sin(-\gamma + \theta) \end{cases} \quad (38)$$

where r is the offset from the primary backbone to the secondary backbone.

4.4 Dynamical model of the continuum robot

The Lagrange equation can be expressed as:

$$\frac{d}{dt} \frac{\partial E_k}{\partial \dot{p}_j} - \frac{\partial E_k}{\partial p_j} + \frac{\partial E_p}{\partial p_j} = Q_j, (j=1,2) \quad (39)$$

where Q_j is the generalized force of system, $p_1 = \beta$ and $p_2 = \gamma$ (as mentioned in Fig. 3).

Substituting Eq. (35) and (36) for Eq. (39), the dynamical equation of the continuum robot can be obtained as:

$$\begin{bmatrix} M_{11} & M_{12} \\ M_{21} & M_{22} \end{bmatrix} \begin{bmatrix} \ddot{\beta} \\ \ddot{\gamma} \end{bmatrix} + \begin{bmatrix} C_{11} & C_{12} & C_{13} \\ C_{21} & C_{22} & C_{23} \end{bmatrix} \begin{bmatrix} \dot{\beta} \\ \dot{\gamma} \end{bmatrix} + \begin{bmatrix} K_{11} & K_{12} \\ K_{21} & K_{22} \end{bmatrix} \begin{bmatrix} \beta \\ \gamma \end{bmatrix} = \begin{bmatrix} D_{11} & D_{12} \\ D_{21} & D_{22} \end{bmatrix} \begin{bmatrix} F_1 \\ F_3 \end{bmatrix} \quad (40)$$

where

$$M_{11} = \frac{1}{3}(4m_1 l^2 K_1 + 3m_1 K_3 + 3m_2 K_6)$$

$$M_{12} = M_{21} = \frac{1}{2} m_1 K_4$$

$$M_{22} = m_1 l^2 K_2 + m_1 K_5 + m_2 K_7$$

$$C_{11} = -\frac{1}{6}(4m_1 l^2 \frac{\partial K_1}{\partial \beta} + 3m_1 \frac{\partial K_3}{\partial \beta} + 3m_2 \frac{\partial K_6}{\partial \beta})$$

$$C_{12} = -\frac{1}{2} m_1 \frac{\partial K_4}{\partial \beta}$$

$$C_{13} = -\frac{1}{2}(m_1 l^2 \frac{\partial K_2}{\partial \beta} + m_1 \frac{\partial K_5}{\partial \beta} + m_2 \frac{\partial K_7}{\partial \beta})$$

$$C_{21} = -\frac{1}{2} m_1 \frac{\partial K_3}{\partial \gamma}$$

$$C_{22} = -\frac{1}{2} m_1 \frac{\partial K_4}{\partial \gamma}$$

$$C_{23} = -\frac{1}{2} m_1 \frac{\partial K_5}{\partial \gamma}$$

$$K_{11} = \frac{4EI}{l}$$

$$K_{12} = K_{21} = K_{22} = 0$$

$$D_{11} = r \cos(\gamma)$$

$$D_{12} = r \cos(\gamma - \frac{2}{3}\pi)$$

$$D_{21} = -r \beta \sin(\gamma)$$

$$D_{22} = -r \beta \sin(\gamma - \frac{2}{3}\pi)$$

5. Simulation examples

To underline the validity of the proposed kinematic and dynamical models, we present some simulation results obtained for the continuum robot using Matlab7.0. The parameters of the simulated continuum robot are given in Table 1. These values correspond to the robot in Fig. 3 and for the rest of this paper.

m_1/g	m_2/g	l/mm	r/mm	h/mm	E/GPa	I/mm^4
1.086	0.848	150	3	15	65	0.102

Table 1. Parameters of the continuum robot.

The pre-set end trajectory of the continuum robot in a base disk coordinate system is given as follows:

$$\begin{cases} x = R \cos(\Omega t) \\ y = R \sin(\Omega t) \\ z = h_z \end{cases} \quad (41)$$

where $R=71.62\text{mm}$ is the radius of the circle, $\Omega=\pi/6$ (rad/s) is the sports angular velocity and $h_z=124.05\text{mm}$ is the height of the circle plane in the Z direction.

For the given end trajectory of the continuum robot in a base disk coordinate system, the movement of all the driven components can be obtained through the kinematics analysis and the driven force can be obtained through dynamics analysis. The initial position of the robot is perpendicular to the base disk (the central axis of the robot coincides with the Z-axis direction). According to the special structure of the continuum robot, the trajectory of the continuum robot should be simulated in two steps: (1) bending simulation and (2) circle simulation.

(1) Bending simulation

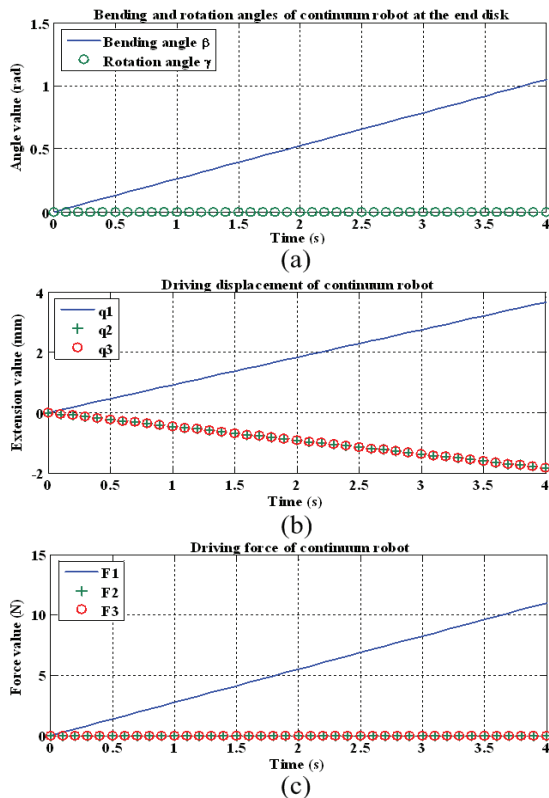


Figure 11. Joint angles, driving displacement and driving force for the planar simulation.

In this step, the end point of the continuum robot will be pulled to the given circle path position by only one secondary backbone. Fig. 11 shows the joint angles, driving displacement and the driving force for the two-dimensional simulation. The results show that when the continuum robot is bending at uniform speed, its driving force is linear to the time. The bending angular

velocity v_β is $\pi/12$ rad/s and the rotation angular velocity v_γ is 0.

(2) Circle simulation

In this step the secondary backbones of the continuum robot should act to drive the end disk to a certain pose. Fig. 12 shows joint angles, driving displacement and driving force for the three dimensional space simulations. The results show that only one or two driven forces are needed to drive the robot to a certain position and the result corresponds to the DOF of the continuum robot. The bending angular velocity v_β is 0 and the rotation angular velocity v_γ is $\pi/6$ rad/s.

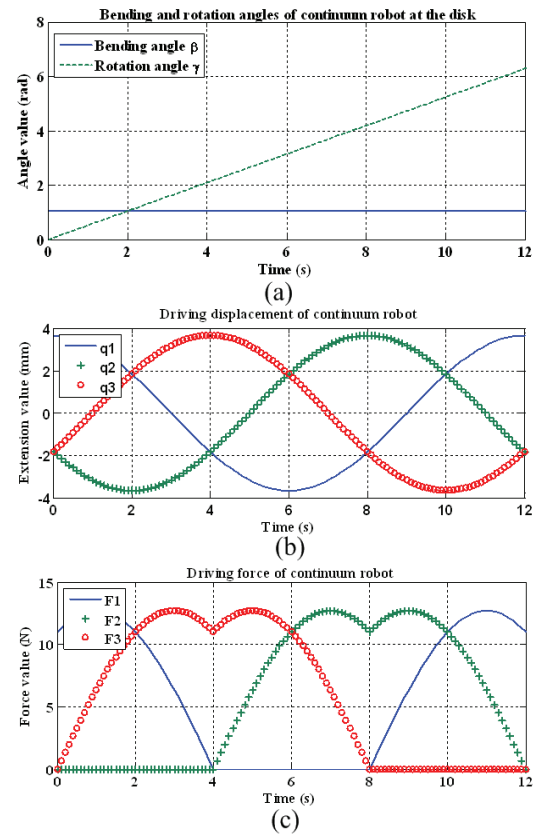


Figure 12. Joint angles, driving displacement and driving force for the 3 dimensional space simulation.

6. Experiments

The prototype of the continuum robot is shown in Fig. 13. The length of the continuum robot is 150mm and its diameter is 10mm. The robot can bend $\pm 180^\circ$ in any direction. The primary and secondary backbones are made of super elastic NiTi wires with 1.2mm diameters. The secondary backbones are connected with three stepping motors which provide the driving force for the continuum robot. The tension sensor is used to measure the driving force provided by the motors. The motion ability of the continuum robot was tested to prove the feasibility of the analytic method for kinematics and dynamics.

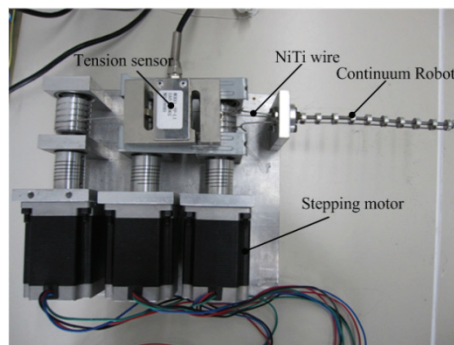


Figure 13. Photo of the prototype.

6.1 Bending ability experiment of the robot

The continuum robot has two DoF, which are bending angle β and rotation angle γ . The experiment is carried out in two-dimensional space (rotation angle $\gamma = 0$) with one secondary backbone applying the driving force. Fig. 14 shows the process of the experiment. The length of the square is 5mm. The figure indicates that the maximum bending angle of the robot is 180° .

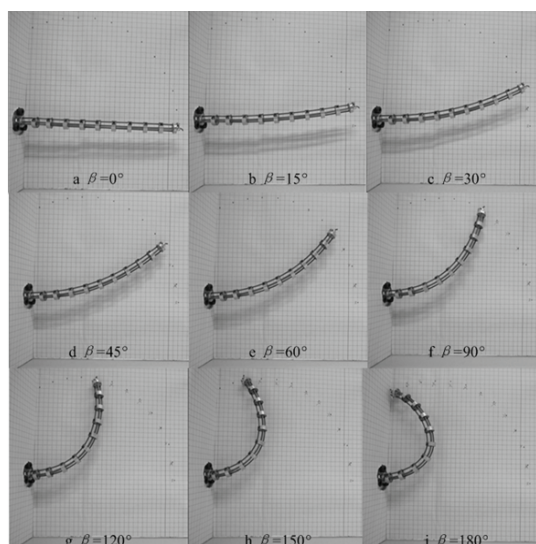


Figure 14. The bending ability experiment of the continuum robot.

Fig. 15 shows the error curve between the theoretical trajectory and the actual trajectory of the end of the robot. The desired trajectory was drawn on the coordinate paper, which was divided into 15 sections equally by 13 points. The robot was driven to bend from 0° to 180° . There was a pen on the end of the robot, so the actual trajectory can be drawn on the paper during the process. We can estimate the errors by measuring the distance between the desired trajectory and actual trajectory at every pre-set point. The result shows the maximum error is no larger than 5mm, which means the relative error is less than 4% of the robot length. Reasons for the error include: (1) manufacture and assembly error, (2) measurement error and (3) the deformation of the NiTi wires.

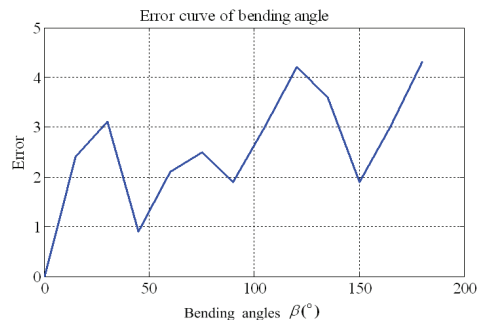


Figure 15. Error between theoretical trajectory and the actual trajectory.

6.2 Driving force experiment of the robot

The pre-set end trajectory of the continuum robot is the circle defined by Eq. 41 and mentioned in Section 5. The driving forces are measured by the tension sensor and its signal is recorded by the computer. The experiment is also divided into two steps: (1) bending experiment and (2) circle experiment.

(1) Bending experiment

In this step, the end point of the continuum robot will be pulled to the given circle path position by one NiTi wire with the driving force of F_1 . Fig. 16 shows the theoretical value, actual value of F_1 and the errors between them. The result shows that the theoretical value of the driving force is less than the actual value, which indicates that the secondary backbone has an initial pretension force in the free state. In addition, because of the friction between the NiTi wires and disks, the error will increase with the increasing driving force.

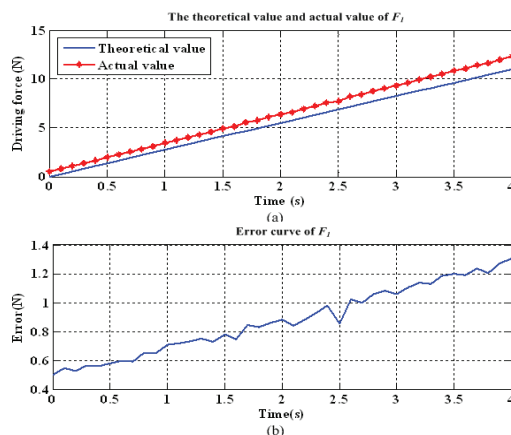


Figure 16. Comparison between theoretical value and actual value of F_1 .

(2) Circle experiment

In this step, the secondary backbones of the continuum robot will drive the end disk to track the pre-set trajectory. The process of the experiment is shown in Fig. 17. The bending angle β remains at 30° and the velocity of rotation angle v_γ is $\pi/6$ rad/s.

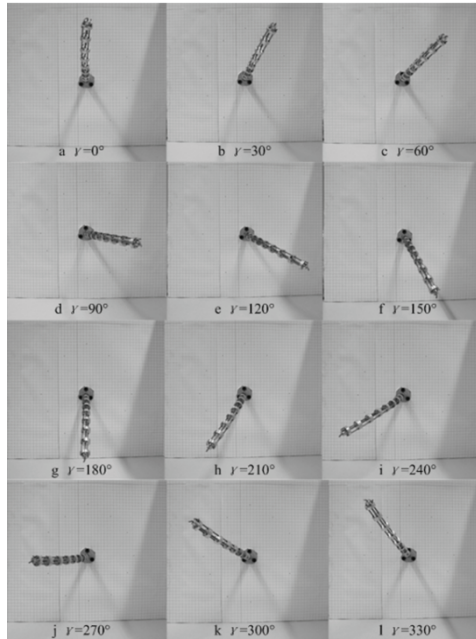


Figure 17. The circle experiment of the continuum robot.

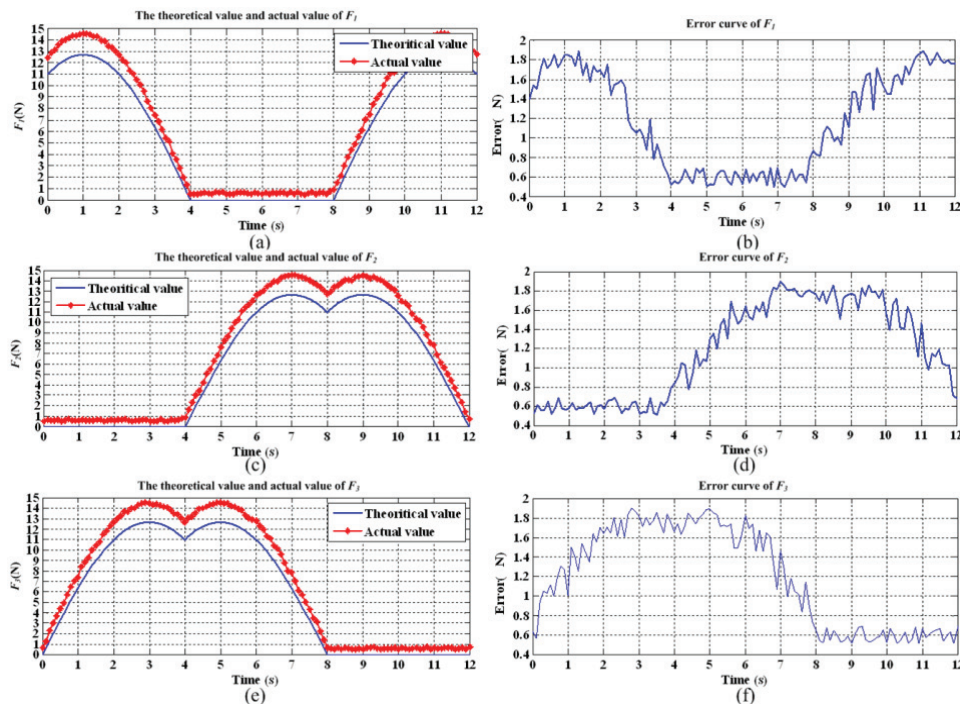


Figure 18. Comparison between theoretical value and actual value of F_i ($i=1, 2, 3$).

7. Conclusion

In this paper an analytic method for the kinematics and dynamics of a new type of continuum robot with multiple flexible backbones has been derived. With consideration of the large deformation character of the flexible backbone, the deformation curve of the flexible beam was obtained on the basis of the Euler-Bernoulli beam equation. Then the kinematic model was formulated on the basis of the deformation. The

Fig. 18 shows the theoretical value, the actual value of F_i ($i=1, 2, 3$) and the errors between them. The results show that the actual driving forces were approximately consistent with the theoretical value, which proves the feasibility of the dynamical model mentioned in Section 4. However, there are small errors between the theoretical value and the actual value. The main reasons for the errors include: (1) omitting the friction between the NiTi wires and disks and (2) the robot has a pretension force and the force is about 0.5N.

dynamical model is derived by using the Lagrange method. The simulation and experimental results demonstrated that the kinematics analysis approach can accurately predict the shape of the continuum robot. The results of the bending ability experiment showed that the maximum error was less than 5mm, or less than 4% of the total robot length. The driving force results also showed that the actual driving forces were approximately consistent with the theoretical driving forces and validated the dynamical model.

The methods developed in this paper can be a useful design tool and also provide the theoretical foundations for control algorithms for continuum robots with multiple-backbones. However, much work remains in the modelling, design and control of continuum robots. Future work includes the study of the deformation characteristic and the stiffness of the robot with an external load, which is an important step forward for future practical applications. The extension of our model should take the friction and pretension force of the backbone into consideration. In addition, the feedback control of the robot should be addressed. On the basis of the two-DoF unit, the kinematics and dynamical model of multiple-DoF continuum robot will be studied.

8. Acknowledgements

The work was supported by National Basic Research Program of China (Grant No. 2011CB013800); National Natural Science Foundation of China (Grant No. 51145013, 51275360); Basic Research Project of Shanghai Science and Technology Commission (Grant No. 11JC1412100).

9. References

- [1] G. Robinson and J. B. C. Davies, "Continuum robots - a state of the art," *Proceedings of IEEE International Conference on Robotics and Automation*, Detroit, Michigan, May 1999, vol. 4, pp. 2849-2854.
- [2] W. Wang, W. Yu and H. Zhang, "JL-2: A Mobile Multi-robot System with Docking and Manipulating Capabilities," *International Journal of Advanced Robotic Systems*, 2010, vol. 7, no. 1, pp. 9-18.
- [3] S. M. Rezaei, F. Barazandeh, M. S. Haidarzadeh, and S. M. Sadat, "The effect of snake muscular system on actuators' torque," *Journal of Intelligent and Robotic Systems*, 2010, vol.59, no.3, pp.299-318.
- [4] J. Casper and R. R. Murphy, "Human-robot interactions during the robot-assisted urban search and rescue response at the World Trade Center," *IEEE Transactions on Systems, Man, and Cybernetics*, 2003, vol. 33, no. 3, pp. 367-385.
- [5] H. Zhang, W. Wang, Z. Deng, G. Zong and J. Zhang, "A novel reconfigurable robot for urban search and rescue," *International Journal of Advanced Robotic Systems*, 2006, vol. 3, no. 4, pp. 359-366.
- [6] A. Ghanbari and S. Noorani, "Optimal trajectory planning for design of a crawling gait in a robot using genetic algorithm," *International Journal of Advanced Robotic Systems*, 2011, vol. 8, no. 1, pp. 29-36.
- [7] N. Simaan, "Snake-like units using flexible backbones and actuation redundancy for enhanced miniaturization," *Proceedings of IEEE International Conference on Robotics and Automation*, Barcelona, Spain, April 2005, pp. 3023-3028.
- [8] K. Xu and N. Simaan, "An Investigation of the Intrinsic Force Sensing Capabilities of Continuum Robots," *IEEE Transactions on Robotics*, 2008, vol.24, no.3, pp.576-587.
- [9] K. Xu and N. Simaan, "Intrinsic wrench estimation and its performance index for multisegment continuum robots," *IEEE Transactions on Robotics*, 2010, vol. 26, no. 3, pp. 555-561.
- [10] B. A. Jones and I. D. Walker, "Kinematics for multisection continuum robots," *IEEE Transactions on Robot*, 2006, vol. 22, no. 1, pp. 43-55.
- [11] D. Trivedi, C. D. Rahn, W. M. Kierb and I. D. Walker, "Soft robotics: Biological inspiration, state of the art, and future research," *Applied Bionics and Biomechanics*, 2008, vol. 5, no. 3, pp. 99-117.
- [12] I. D. Walker, C. Carreras, R. McDonnell and G. Grimes, "Extension versus Bending for Continuum Robots," *International Journal of Advanced Robotic Systems*, 2006, vol. 3, no. 2, pp. 171-178.
- [13] M. W. Hannan and I. D. Walker, "Kinematics and the implementation of an elephant's trunk manipulator and other continuum style robots," *Journal of Robotic Systems*, 2003, vol. 20, no. 2, pp. 45-63.
- [14] I. A. Gravagne and I. D. Walker. "Manipulability, force, and compliance analysis for planar continuum manipulators," *IEEE Transactions on Robotics and Automation*, 2002, vol.18, no.3, pp.263-273.
- [15] K. Xu and N. Simaan. "Analytic Formulation for Kinematics, Statics, and Shape Restoration of Multibackbone Continuum Robots Via Elliptic Integrals," *ASME Journal of Mechanisms and Robotics*, 2010, vol. 2, no. 2, pp. 011006-1-011006-13.
- [16] R. J. Webster III, J. M. Romano, and N. J. Cowan. "Mechanics of precurved-tube continuum robots," *IEEE Transactions on Robotics*, 2009, vol.25, no.1, pp. 67-78.
- [17] R. J. Webster III, J. M. Romano, and N. J. Cowan. "Kinematics and calibration of active cannulas," *Proceedings of IEEE International Conference on Robotics and Automation*, Pasadena, CA, USA, 2008, pp.3888-3895.
- [18] D. C. Rucker and R. J. Webster III, "Statics and dynamics of continuum robots with general tendon routing and external loading," *IEEE Transactions on Robotics*, 2011, vol.27, no.6, pp.1033-1044.
- [19] R. J. Webster III and B. A. Jones, "Design and kinematic modelling of constant curvature continuum robots: a review," *International Journal of Robotics Research*, 2010, vol.29, no.13, pp.1661-1683.
- [20] D. Trivedi, A. Lotfi and C. Rahn, "Geometrically exact models for soft robotic manipulators," *IEEE Transactions on Robotics*, 2008, vol. 24, no. 5, pp. 773-780.
- [21] G. S. Chirikjian. "Hyper-redundant manipulator dynamics: a continuum approximation," *Advanced Robotics*, 1995, vol.9, no.3, pp.217-243.
- [22] F. Matsuno and H. Sato, "Trajectory Tracking Control of Snake Robots Based on Dynamic Model,"

- Proceedings of IEEE International Conference of Robotics and Automation*, Barcelona, Spain, 2005, pp. 3040-3045.
- [23] I. A. Gravagne, I. D. Walker, and C. D. Rahn, "Large-Deflection Dynamics and Control for Planar Continuum Robots," *IEEE/ASME Transactions on Mechatronics*, 2003, vol.37, no.2, pp.299-307.
- [24] I. A. Gravagne and I. D. Walker, "Good vibrations: A vibration damping setpoint controller for continuum robots," *Proceedings of IEEE International Conference of Robotics and Automation(ICRA)*, Seoul, Korea, 2001, pp.3877-3884.
- [25] H. Mochiyama and T. Suzuki. "Dynamics modelling of a hyper-flexible manipulator," *Proceedings of the 41st SICE Annual Conference*, Osaka, 2002, pp.1505-1510.
- [26] H. Mochiyama and T. Suzuki. "Kinematics and dynamics of a cable-like hyper-flexible manipulator," *Proceedings of IEEE International Conference of Robotics and Automation*, Taipei, 2003, pp.3672-3677.
- [27] E. Tatlicioglu, I. D. Walker, and D. M. Dawson. "Dynamic modelling for planar extensible continuum robot manipulators" *Proceedings of IEEE International Conference on Robotics and Automation*, Roma, 2007, pp.1357-1362.
- [28] E. Tatlicioglu, I. D. Walker, and D. M. Dawson. "New Dynamic Models for Planar Extensible Continuum Robot Manipulators," *Proceedings of the 2007 IEEE/RSJ International Conference on Intelligent Robots and Systems*, San Diego, CA, USA, 2007, pp.1485-1490.
- [29] S. Nemat-Nasser and W.-G. Guo. "Superelastic and Cyclic Response of NiTi SMA at Various Strain Rates and Temperatures," *Mechanics of Materials*, 2006, vol.38, no.5-6, pp. 463-474.
- [30] L. L. Howell. *Compliant mechanism*. McGraw Hill, New York, 2001.
- [31] D.G. Fertis, *Advanced Mechanics of Structure*. Marcel Dekker, inc., New York City, 1996.